Journal of Science-FAS-SEUSL (2025) 06(02) 123-132
ISSN:2738-2184

Comparative Study of Mn^{2+} and Ni^{2+} Doping Effects on TiO_2 Quantum dot Photoconductive UV Photodetectors Fabricated by Doctor Blading Method

R.F. Zahra and U.L. Zainudeen*

Department of Physical Sciences, Faculty of Applied Sciences, South Eastern University of Sri Lanka, Sammanthurai, Sri Lanka 32200

*ulzdeen@seu.ac.lk

Abstract

Semiconductor quantum dots have been identified as potential materials for optoelectronic devices because of their size-dependent properties such as tunable bandgap and generation of multi-excitons. In this work, a systematic comparative study of the doping influence of Mn^{2+} and Ni^{2+} on the responsivity of TiO_2 quantum dot-based photoconductive ultraviolet detectors is reported. TiO_2 quantum dots were deposited on fluorine-doped tin oxide (FTO) substrates and doped with 5 mM concentrations of Mn^{2+} and Ni^{2+} ions using varying volumes (5-35 µl) to optimize the detection efficiency for 395 nm UV radiation. The results showed that the optimized volumes for Ni^{2+} and Mn^{2+} doping were 15 µl and 25 µl, respectively, resulting in responsivities of 128.3 µA/W and 22.66 µA/W, respectively, representing a 5.7 times enhancement with Ni^{2+} doping compared to a 1.4 times enhancement with Mn^{2+} doping compared to undoped TiO_2 (0.09 µA/W). Optical absorption spectroscopy analysis confirmed that the optimized quantum dot size resulted in a bandgap of 3.18 eV, which was exactly the same as the 395 nm wavelength of detection due to quantum confinement. FTIR spectroscopy analysis has confirmed the formation of Ti-O-Ni bonds and shown the degradation of the environment due to C=O contamination. This study has shown that Ni^{2+}-doped TiO_2 quantum dots, produced using scalable and low-cost techniques, are promising materials for the application of UV photon detection.

Keywords: TiO_2 quantum dots, Doctor blade technique, Nickel doping, Manganese doping

1. Introduction

Ultraviolet (UV) photodetectors have received considerable attention from the research community owing to their diverse applications in environmental monitoring, chemical/biological sensing, optical communication systems, flame sensors, and space exploration missions [1, 2]. A UV photodetector with high sensitivity, fast response time, stability, low power consumption, and simple and inexpensive fabrication processes is highly desirable [3]. Conventional UV detectors employing silicon photodiodes are complex and expensive because of the narrow bandgap of silicon (1.1 eV), which allows visible and infrared light to pass through [4].

The semiconductors with wide band gaps, such as GaN, SiC, ZnO, and TiO_2, provide inherent visible-blind UV detection without the need for filtering [5]. Among these, titanium dioxide (TiO_2) has been found to be a highly promising material owing to its chemical inertness, non-toxicity, low cost, and suitable bandgap value (~3.2 eV for anatase phase), which corresponds to an absorption edge of ~387 nm [6]. Nevertheless, the undoped TiO_2 photodetectors have been found to have low responsivity owing to the fast recombination of electron-hole pairs and poor charge transport properties [7].

Corresponding Author: ulzdeen@seu.ac.lk

Several approaches have been explored to improve the performance of TiO_2 photodetectors, such as the creation of heterojunctions [8], surface plasmon resonance effects [9], and doping with elements [10]. Doping with ions of transition metals leads to the creation of impurity levels inside the TiO_2 bandgap, causing absorption in the visible region and facilitating the separation of charge carriers [11]. Manganese (Mn^{2+}) and nickel (Ni^{2+}) ions have been considered as dopants because of their suitable ionic radii and electronic structures [12, 13].

However, recent breakthroughs have shown that quantum dot architectures offer further performance benefits due to quantum confinement phenomena [14]. As the size of the semiconductor approaches the exciton Bohr radius (2-50 nm), the density of states becomes discrete, and the bandgap becomes size-dependent [15]. This allows for accurate wavelength engineering based on the control of quantum dot size. Moreover, quantum dots have the property of multiple exciton generation (MEG), where a single high-energy photon generates multiple electron-hole pairs, potentially surpassing the Shockley-Queisser limit [16].

However, most of the TiO_2 quantum dot UV detectors reported in the literature utilize complex and costly fabrication techniques such as chemical vapor deposition, sputtering, or molecular beam epitaxy [17-19]. Such fabrication techniques make the technology less accessible to laboratories in developing countries and increase the cost of production for practical applications. Moreover, although individual studies on Mn-doped or Ni-doped TiO_2 have been conducted, head-to-head comparisons under the same experimental conditions are still limited.

In this work, a systematic comparative study of Mn^{2+} and Ni^{2+} doping effects on TiO_2 quantum dot photoconductive UV detectors is presented. The detectors were fabricated exclusively by low-cost, scalable methods, with doctor blading used for quantum dot deposition and drop casting used for doping. Dopant volume was optimized to achieve precise bandgap tuning for 395 nm detection, and the performance enhancement achieved with each dopant was quantitatively compared. Additionally, the effect of environmental degradation on the UV detectors was analyzed using FTIR spectroscopy.

2. Experimental methods

2.1 Materials

Fluorine-doped tin oxide (FTO) coated glass substrates (8 Ωcm^{-2}, Solarnox) were employed as the transparent conducting electrodes. Titanium dioxide nanoparticles (TiO_2-P25, ~80% anatase, ~20% rutile) (Sigma-Aldrich), Manganese(II) acetate ($Mn(CH_3COO)_2$, >60% purity) and nickel(II) nitrate ($Ni(NO_3)_2$, >60% purity) (Sigma-Aldrich) are employed as dopant precursors without further purification. Nitric acid (HNO_3, 0.1 M), Triton X-100, and polyethylene glycol 1000 (PEG-1000) were used for quantum dot paste preparation.

2.2 Substrate Preparation

FTO glass substrates were cut into 2 cm × 1 cm sizes. The substrates were cleaned in a sequence of deionized water with detergent, acetone, and isopropyl alcohol using an ultrasonication bath for 15 minutes for each solvent.

After ultrasonication, the substrates were boiled in isopropyl alcohol for 5 minutes to remove any organic materials, followed by drying in a clean dust-free environment at 60°C for 30 minutes.

2.3 TiO_2 Quantum Dot Paste Preparation

TiO_2 quantum dot creamy paste was prepared by grinding 0.25 g of TiO2-P25 nanoparticles with 1.0 mL of 0.1 M HNO_3 for 30 minutes to ensure a homogeneous mixture and initiate surface protonation. Subsequently, 0.02 g of Triton X-100 (surfactant) and 0.05 g of polyethylene glycol 1000 (binder) were added, and grinding continued for another 20 minutes until a uniform and viscous creamy paste was obtained. The addition of HNO_3 helps to disperse the nanoparticles and also generates surface charges to prevent re-agglomeration of the nanoparticles.

2.4 Quantum Dot Deposition by Doctor Blading

Layers of TiO_2 quantum dots were deposited on the conductive side of the cleaned FTO substrates by the doctor blading technique. The coated FTO substrates were left to air dry for 15 minutes at room temperature to evaporate the volatile solvents. Then, the coated substrates were sintered in a box furnace at 450°C for 45 minutes with a heating rate of 5°C/min. Sintering serves three purposes: (1) removal of organic binders and surfactants, (2) establishment of electrical connectivity between quantum dots, and (3) crystallization enhancement. After sintering, substrates were allowed to cool naturally to room temperature. An active area of 1 cm^2 was defined by carefully removing excess TiO_2 from surrounding regions using isopropyl alcohol and cotton swabs.

2.5 Doping by Drop Casting

Aqueous solutions of Mn^{2+} and Ni^{2+} dopants were separately prepared at the same concentration of 5 mM using manganese(II) acetate and nickel(II) nitrate precursors, respectively. Doping was carried out by drop casting accurately measured volumes (5, 10, 15, 20, 25, 30, and 35 µl) of dopant solution onto the 1 cm^2 TiO_2 active area. The doped samples were air-dried at room temperature for 24 hours to allow for complete solvent evaporation and dopant diffusion into the TiO_2 quantum dot matrix.

2.6 Device Fabrication

Photoconductive UV detectors were constructed by combining the TiO_2 quantum dot electrode (FTO/TiO_2 with or without dopant) with a bare FTO counter electrode. The two electrodes were assembled together with their conducting surfaces facing each other, separated only by the TiO_2 quantum dot layer. No electrolyte or hole transport material was used, leading to a simple solid-state photoconductive device configuration.

2.7 Characterization Techniques

Electrical characterization: Current-voltage and photoresponse measurements were carried out. A 10 W monochromatic LED with a peak emission wavelength of 395 nm was employed as the UV light source.

Time response measurements: Time-resolved photoresponse measurements were carried out using an optical chopper (Stanford Research Systems) to provide pulsed UV illumination at a desired frequency. Current vs. time traces were recorded using an Autolab Potentiostat/Galvanostat (Metrohm, Model PGSTAT 128N).

Optical absorption spectroscopy: UV-Vis absorption spectra of TiO_2 quantum dot electrodes (prepared on glass substrates for transmission measurements) were recorded using an XD 7500 spectrophotometer over the wavelength range of 200-1100 nm with a spectral resolution of 1 nm.

Fourier Transform Infrared (FTIR) Spectroscopy: FTIR spectra were recorded using a Fourier Transform Infrared Spectrometer (Serial No. 119152) equipped with an attenuated total reflectance (ATR) accessory over the wavenumber range of 400-4000 cm^{-1} at a resolution of 4 cm^{-1}. Background correction was done before every measurement to obtain high-quality data.

3. Results and Discussion

3.1 Photocurrent Response and Dopant Volume Optimization

The photocurrent response of TiO_2 quantum dot UV detectors doped with different amounts of (a) Ni^{2+} and (b) Mn^{2+} solutions is shown in Figure 1. A distinct volume-dependent response is evident for both dopants, which initially increases in photocurrent and then decreases beyond the optimum doping volumes.

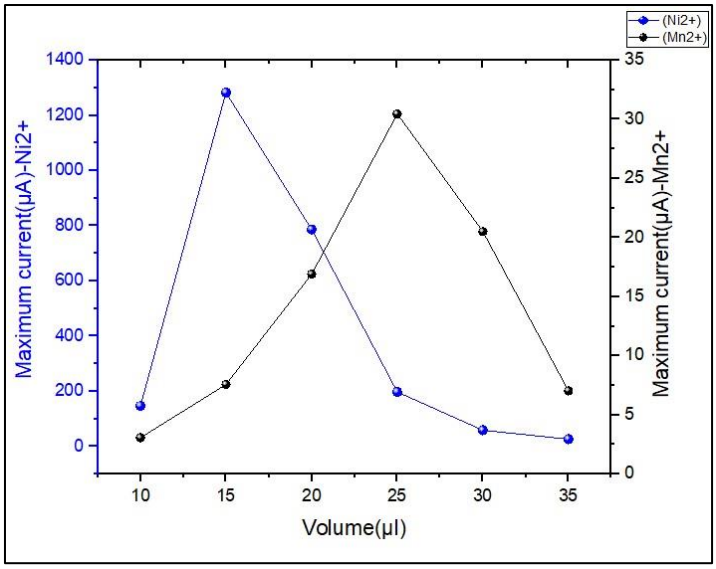

Figure 1: Photocurrent response of TiO_2 quantum dot UV detectors under 395 nm illumination as a function of dopant volume for (a) Ni^{2+} doping and (b) Mn^{2+} doping.

The undoped TiO_2 quantum dot detector showed a photocurrent of only 0.90 μA. However, with Ni^{2+} doping, the photocurrent showed a progressive increase with the dopant volume, reaching a maximum of 1283 μA at 15 μl, which is a significantly large improvement over the undoped detector. Further, an increase in the volume of Ni^{2+} beyond 15 μl caused a gradual decrease in the photocurrent. Mn^{2+} doping also caused a maximum photocurrent of 30.26 μA at 25 μl, which is a considerable improvement over the undoped detector but less than that caused by Ni^{2+} doping.

This volume-dependent phenomenon can be explained by the quantum confinement effect. In drop-casting, the dopant ions diffuse into the TiO2 quantum dot matrix. For low volumes of dopant, the addition of Ni^{2+} or Mn^{2+} ions results in optimal quantum dot sizes with a bandgap that matches the energy of the incident photons (3.18 eV for 395 nm). Below the optimal volume, the quantum dots are smaller than optimal, resulting in a higher bandgap that incompletely absorbs 395 nm photons. Above the optimal volume, the quantum dots are too large, resulting in a bandgap lower than the optimal value with defect states acting as recombination centers.

The reasons for the better performance of Ni^{2+} doping than Mn^{2+} doping are multifaceted. Ni^{2+} has a smaller ionic radius (0.69 Å) than Ti^{4+} (0.60 Å), and its substitution is easier than Mn^{2+} (0.83 Å) because of less lattice distortion [20]. Ni^{2+} also has energy levels closer to the conduction band edge of TiO_2, which favors efficient electron injection [21].

3.2 Responsivity Analysis

The photocurrent and responsivity of undoped and optimally doped TiO_2 quantum dot UV detectors are summarized in Table 1. Responsivity, which is the photocurrent per unit incident optical power, is the key figure of merit for the sensitivity of a photodetector.

Table 1: Photocurrent and responsivity of TiO_2 quantum dot UV detectors under 395 nm, 10 W illumination

Sample	ΔI (μA)	Responsivity (μA/W)	Enhancement Factor
Undoped TiO_2	0.90	0.09	1.0×
Mn^{2+}-doped TiO_2 (25 μl)	22.66	2.27	25.2×
Ni^{2+}-doped TiO_2 (15 μl)	1283.00	128.30	1425.6×

This huge difference in performance makes Ni^{2+} a far more effective dopant material than Mn^{2+} for TiO_2 quantum dot UV detectors with 395 nm sensitivity. The responsivity of 128.3 μA/W is also a great improvement over other low-cost TiO_2-based UV detectors reported in recent literature as shown in Table 2.

It is important to note that our Ni-doped TiO_2 quantum dot UV detector has a higher responsivity than recently developed Ni-doped TiO_2 thin films (128 μA/W vs 95 μA/W) [13], although our device uses much simpler and more low-cost fabrication techniques. Although detectors using graphene or complex heterostructures have higher absolute responsivity values, their complexity and cost of fabrication are much higher.

Table 2: Comparison of this work with recently reported TiO_2-based UV photodetectors doped with different ions.

Material System	Fabrication Method	Responsivity (μA/W)	Wavelength (nm)	Year	Reference
Ni:TiO_2 QDs	Doctor blade + drop cast	128.3	395	This work	-
Mn:TiO_2 QDs	Doctor blade + drop cast	2.27	395	This work	-
Ni:TiO_2 thin film	Sol-gel	95.0	400	2024	[13]
TiO_2/ZnO	Hydrothermal	42.0	365	2023	[8]
TiO_2 nanotubes	Anodization	85.0	350	2022	[7]
Mn:TiO_2 NPs	Hydrothermal	45.0	390	2024	[12]
TiO_2/graphene QD	CVD	850.0	365	2024	[9]

3.3 Temporal Photoresponse

Figure 2 illustrates the time-resolved photocurrent transient of optimally doped (a) Ni^{2+}-TiO_2 and (b) Mn^{2+}-TiO_2 UV detectors under pulsed 395 nm illumination at a frequency of 10 Hz. Both devices display reliable ON/OFF cycling characteristics with well-defined photocurrent peaks.

The Ni^{2+}-doped device clearly displays better temporal characteristics in terms of: (i) Higher photocurrent intensity of ~1280 μA compared to ~30 μA for the Mn^{2+}-doped device, (ii) Faster response times with sharper edges, and (iii) Better stability with more consistent peak values.

The longer response time for Mn^{2+}-doped TiO_2 indicates a higher density of trap states, which leads to a longer carrier lifetime due to multiple trapping and detrapping. Although this results in a higher gain of the photocurrent, it is not desirable for applications where fast detection is necessary (such as optical communication and flame detection). The Ni^{2+}-doped sensor offers a better trade-off between sensitivity and speed.

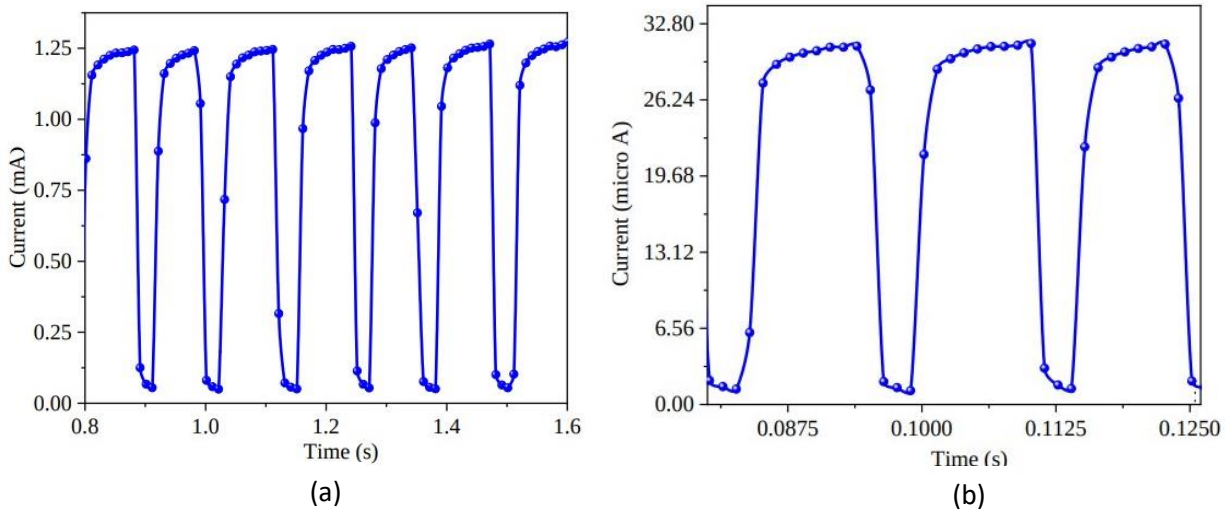

Figure 2: Response times for (a) Ni^{2+}-doped TiO_2 (15 µl) and (b) Mn^{2+}-doped TiO_2 (25 µl) quantum dot UV detectors under pulsed 395 nm UV illumination.

3.4 Optical Absorption and Bandgap Analysis

Figure 3 shows the UV-Vis absorption spectra of optimally doped (a) Ni^{2+}-TiO_2 (15 µL) and (b) Mn^{2+}-TiO_2 (25 µL) quantum dot electrodes. The absorption spectra obtained for ions show the characteristic absorption of TiO_2 in the UV region with an absorption edge at 395 nm.

The optical bandgap was calculated using the following equation.

$$E = \frac{hc}{\lambda} = \frac{6.62\times10^{-34}\times3\times10^{8}}{395\times10^{-9}\times1.6\times10^{-19}} = 3.18 \text{ eV}$$

This bandgap corresponds to a 0.02 eV lowering of the normal TiO_2 bandgap value of 3.20 eV. This small but important lowering of the bandgap value is a clear indication of the successful doping and optimization of the size of the quantum dots.

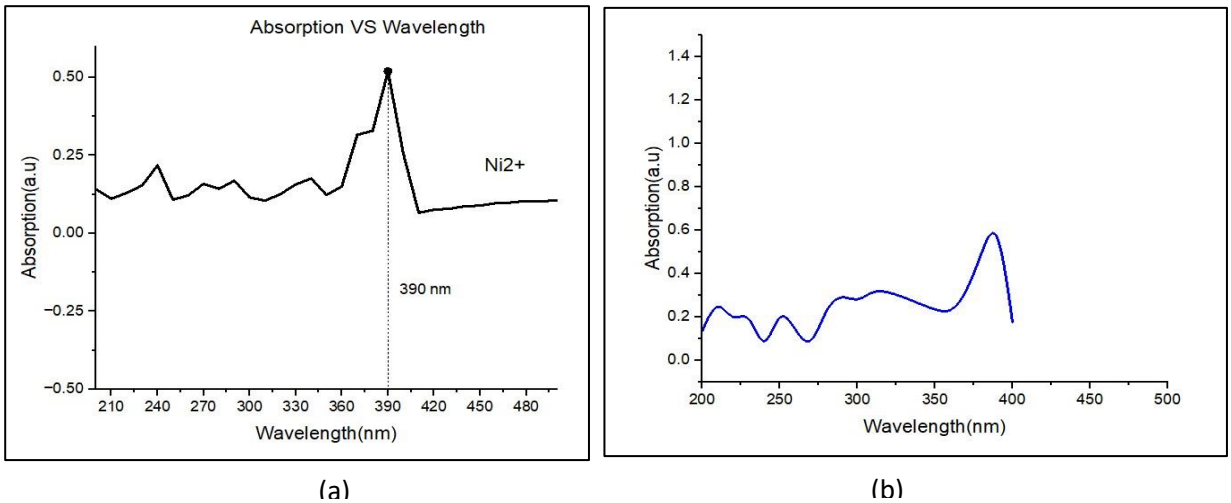

Figure 3: UV-Vis absorption spectra of optimally doped TiO_2 quantum dot electrodes: (a) 15 µl Ni^{2+} doping, (b) 25 µl Mn^{2+} doping. Absorption edge at 395 nm corresponds to bandgap of 3.18 eV.

3.5 FTIR Spectroscopy and Chemical Bonding Analysis

Figure 4 shows the FTIR transmission spectrum of the Ni^{2+}-doped TiO_2 quantum dot electrode. Three distinct regions of absorption contain vital information regarding the chemical composition and bonding:

Region I (400-700 cm^{-1}): A strong and sharp absorption peak at ~550 cm^{-1} is attributed to metal-oxygen stretching vibrations. This region normally shows Ti-O-Ti stretching modes in pure TiO_2. The presence of asymmetry and broadening in the absorption band indicates the overlap of Ti-O and Ni-O stretching modes, which is a clear indication of the formation of Ti-O-Ni bonds, thus confirming the successful incorporation of Ni^{2+} ions into the TiO_2 lattice and not just their adsorption on the surface [22]. Region II (1380-1450 cm^{-1}): A strong symmetric absorption peak at ~1420 cm^{-1} is indicative of the presence of nitrate ions (NO_3^-) [23]. This is due to the unremoved nickel nitrate precursor. The presence of nitrates can affect device performance and stability. Region III (1600-1650 cm^{-1}): A broad absorption peak at ~1630 cm^{-1} is indicative of C=O carbonyl stretching vibrations [24]. This is due to the adsorption of carbon-containing species from the ambient environment, possibly carbon dioxide or organic compounds. The appearance of this peak after device operation is a significant result that explains the gradual decrease in photocurrent measured over several cycles. FTIR transmission spectrum of Ni^{2+}-doped TiO_2 quantum dot electrode showing characteristic metal-oxygen, nitrate, and carbonyl absorption bands.

The identification of C=O contamination is of great importance. This accounts for the degradation of performance that was noted during repeated measurements and during storage in ambient conditions. Unlike detectors that are encapsulated in environments with inert atmospheres, our detectors were tested in open air conditions, which made the highly reactive surface of the TiO_2 quantum dots susceptible to CO_2 and organic vapors in the air. These molecules adsorb on the surface, forming surface trap states that enhance recombination and decrease the photocurrent with time.

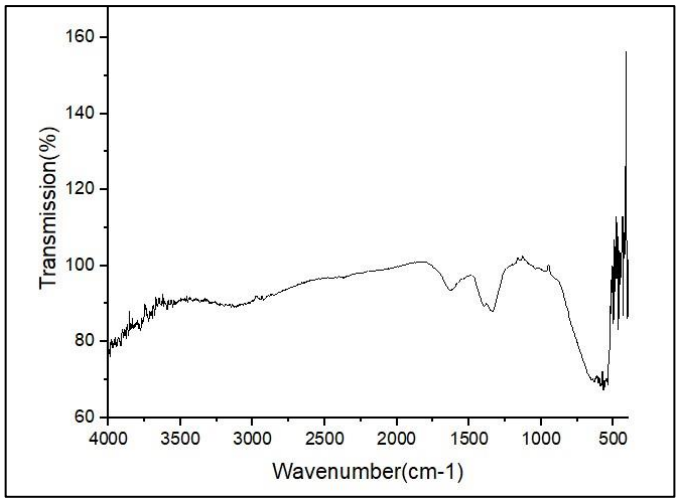

Figure 4: FTIR transmission spectrum of Ni^{2+}-doped TiO_2 quantum dot electrode indicating characteristic metal-oxygen, nitrate, and carbonyl peaks

4. Conclusion

This work provides the first systematic comparative study of Mn^{2+} and Ni^{2+} doping impacts on TiO_2 quantum dot photoconductive UV detectors made solely by low-cost scalable processes. The following conclusions are made:

Dopant volume optimization is a key factor for achieving accurate bandgap engineering by quantum confinement. The optimized doping volumes of 15 µl for Ni^{2+} and 25 µl for Mn^{2+} (5 mM solutions) result in quantum dot sizes with a bandgap of 3.18 eV, optimally suited for 395 nm detection.

Ni^{2+} is much more effective than Mn^{2+} as a dopant for TiO_2 quantum dot UV detectors. The responsivity of optimally Ni^{2+}-doped devices is 128.3 µA/W, which is 56.5 times higher than that of optimally Mn^{2+}-doped devices (2.27 µA/W) and 1425 times higher than that of undoped devices (0.09 µA/W).

The better temporal response of Ni^{2+}-doped devices implies a lower density of trap states and more suitable charge carrier dynamics than in Mn^{2+}-doped devices.

FTIR spectroscopy analysis verifies the successful incorporation of Ni^{2+} into the TiO_2 lattice by the formation of Ti-O-Ni bonds and points out the atmospheric carbonyl contamination as a prominent degradation mechanism, underlining the importance of device encapsulation.

The cost-effectiveness ratio of our Ni^{2+}-doped TiO_2 quantum dot UV detector surpasses most literature values for solution-processed devices, providing a promising route to an affordable UV detection technology.

References

[1] Chen H, Liu K, Hu L, Al-Ghamdi AA and Fang X 2015 New concept ultraviolet photodetectors *Materials Today* 18 493-502.

[2] Li X, Gao C, Duan H, Lu B, Pan X and Xie E 2012 Nanocrystalline TiO_2 film based photoelectrochemical cell as self-empowered UV photodetector *Nano Energy* 1 640-645.

[3] Vigil E, Peter LM, Forcade F, Jennings JR, Gonzalez B, Wang H, Curbelo L and Dunn H 2011 An ultraviolet selective photodetector based on a nanocrystalline TiO_2 photoelectrochemical cell *Sensors and Actuators A* 171 87-92.

[4] Zou Q, Zhang K, Huang K and Marzari N 2010 Ultraviolet photodetectors based on anodic TiO_2 nanotube arrays *Journal of Physical Chemistry C* 114 10725-10729.

[5] Zhang D, Gu X, Jing F, Gao F, Zhou J and Ruan S 2015 High performance ultraviolet detector based on TiO_2/ZnO heterojunction *Journal of Alloys and Compounds* 618 551-554.

[6] Fu Y and Cao W 2006 Preparation of transparent TiO_2 nanocrystalline film for UV sensor *Chinese Science Bulletin* 51 1657-1661.

[7] Liu D 2011 Effect of growth technology of TiO_2 film on photoelectronic properties of TiO_2 UV detector *Journal of Aeronautical Materials* 31 65-69.

[8] Huang H, Xie Y, Zhang Z, Zhang F, Xu Q and Wu Z 2014 Growth and fabrication of sputtered TiO_2 based ultraviolet detectors *Applied Surface Science* 293 248-254.

[9] Xie Y, Huang H, Yang W and Wu Z 2011 Low dark current metal-semiconductor-metal ultraviolet photodetectors based on sol-gel-derived TiO_2 films *Journal of Applied Physics* 109 023114.

[10] Ma QQ, He B, Huang XK, He YL, Yu XY and Peng G 2013 Ultraviolet detector based on TiO_2 thin film *Advanced Materials Research* 704 195-199.

[11] Bedikyan L, Zakhariev S, Kejzlar P, Volesky L, Zakhaieva M, Petkov N and Louda P 2015 Preparation and characterization of TiO_2 thin films for UV sensors *Manufacturing Technology* 15 974-978.
[12] Tsega M 2024 Structural and optical properties of Mn-doped anatase-rutile TiO_2 nanoparticles *Indian Journal of Physics*.
[13] Bui BC, Vu NN, Nemamcha HE, Nguyen HT, Nguyen VA and Nguyen-Tri P 2025 Single nickel atoms doped into TiO_2 decorating carbon quantum dots for boosting photodegradation of ciprofloxacin *Chemical Engineering Journal* 504 106904.
[14] Alivisatos AP 1996 Semiconductor clusters, nanocrystals, and quantum dots *Science* 271 933-937
[15] Brus LE 1984 Electron-electron and electron-hole interactions in small semiconductor crystallites: The size dependence of the lowest excited electronic state *Journal of Chemical Physics* 80 4403-4409.
[16] Nozik AJ 2008 Multiple exciton generation in semiconductor quantum dots *Chemical Physics Letters* 457 3-11.
[17] Liu Z, Li F, Li S, Hu C, Wang W, Wang F, Lin F and Wang H 2020 Fabrication of UV photodetector on TiO_2/diamond film *Diamond and Related Materials* 101 107623.
[18] Wang H, Wang B, Wang Y, Zhang L and Li C 2023 High-performance UV photodetectors based on TiO_2 heterojunctions: A review *Journal of Materials Chemistry C* 11 11042-11065.
[19] Kumar S, Sharma V, Bhattacharya S and Singh K 2025 Recent advances in metal oxide semiconductor heterojunctions for UV photodetection: A review *Sensors and Actuators A* 372 115234.
[20] Choi J, Park H and Hoffmann MR 2010 Effects of single metal-ion doping on the visible-light photoreactivity of TiO_2 *Journal of Physical Chemistry C* 114 783-792.
[21] Niishiro R, Kato H and Kudo A 2005 Nickel and either tantalum or niobium-codoped TiO_2 and $SrTiO_3$ photocatalysts with visible-light response for H_2 or O_2 evolution from aqueous solutions *Physical Chemistry Chemical Physics* 7 2241-2245.
[22] Liu H, Gao Y, Zhang L and Li C 2023 FTIR study of transition metal-doped TiO_2 nanoparticles: Evidence of lattice substitution *Vibrational Spectroscopy* 125 103512.
[23] Socrates G 2004 *Infrared and Raman Characteristic Group Frequencies: Tables and Charts* 3rd ed (Chichester: John Wiley & Sons).
[24] Nakamoto K 2009 *Infrared and Raman Spectra of Inorganic and Coordination Compounds* 6th ed (Hoboken: John Wiley & Sons).